ELSEVIER

Journal of Hazardous Materials 142 (2007) 315–323

Journal of Hazardous Materials

www.elsevier.com/locate/jhazmat

Air flow paths and porosity/permeability change in a saturated zone during in situ air sparging

Yih-Jin Tsai *

Department of Environment and Resources Engineering, Diwan College of Management, No. 87-1, Nansh Li, Madou, Tainan, Taiwan

Received 1 November 2005; received in revised form 27 June 2006; accepted 10 August 2006
Available online 12 August 2006

Abstract

This study develops methods to estimate the change in soil characteristics and associated air flow paths in a saturated zone during in situ air sparging. These objectives were achieved by performing combined in situ air sparging and tracer testing, and comparing the breakthrough curves obtained from the tracer gas with those obtained by a numerical simulation model that incorporates a predicted change in porosity that is proportional to the air saturation. The results reveal that revising the porosity and permeability according to the distribution of gas saturation is helpful in breakthrough curve fitting, however, these changes are unable to account for the effects of preferential air flow paths, especially in the zone closest to the points of air injection. It is not known the extent to which these preferential air flow paths were already present versus created, increased, or reduced as a result of the air sparging experiment. The transport of particles from around the sparging well could account for the overall increase in porosity and permeability observed in the study. Collection of soil particles in a monitoring well within 2 m of the sparging well provided further evidence of the transport of particles. Transport of particles from near the sparging well also appeared to decrease the radius of influence (ROI). Methods for predicting the effects of pressurized air injection and water flow on the creation or modification of preferential air flow paths are still needed to provide a full description of the change in soil conditions that accompany air sparging.

Keywords: Air sparging; Porosity change; Permeability change; Air flow path; Tracer test

1. Introduction

In situ air sparging (IAS) removes volatile organic contaminants from a saturated zone by combining volatilization and aerobic biodegradation. Air is injected below the water table through a slotted screen in a sparging well, and the injected air rises to the vadose zone [1]. The efficiency of IAS for remediation depends strongly on the gas saturation of the aquifer. Both the air flow path and the radius of influence (ROI) may be influenced by the soil characteristics [2–4].

The movement of particles during air sparging was observed in sandbox experiments in an earlier work [5]. The mechanical energy of moving water imposes a shear stress on the soil matrix and releases particles into suspension. Mobile particle concentrations and the mean particle diameter increase with the water flow rate [6,7]. These results may be attributed to two mechanisms. First, the shear stress imposed on the matrix by the moving water increases with flow rate, releasing larger particles into suspension. Second, the particle transporting ability of water increases with flow rate. Noack et al. [8] performed column tests to investigate the vertical mobility of suspended particles and found that fine particles suspensions always leached through the various soil fractions more quickly than the coarser colloid suspensions under similar hydrological conditions.

When the air begins to be injected into the saturated zone, the air displaces the water and induces water flow through the porous medium. Flowing water can transport soil particles during air sparging by means of the shear stress. Tsai and Lin reported the mobilization of sand particles and an increase in the porosity that was directly proportional to the rate at which air was injected.

If soil particles are transported during air sparging, then the distributions of the porosity and the reservoir permeability will change, altering the flow path of the air. Theoretical studies and numerical simulations of air sparging, with reference to air flow paths, have been performed [3,4,9–14], but the effect of particle mobilization on the flow path of air has never been considered.

* Tel.: +886 6 5718888x871; fax: +886 6 5718014.
E-mail address: yjtsai@mail.dwu.edu.tw.

0304-3894/$ – see front matter © 2006 Published by Elsevier B.V.
doi:10.1016/j.jhazmat.2006.08.014

This work couples in situ air sparging with a tracer test to elucidate the behavior of air flow in an aquifer. The application of a tracer gas at the air injection well and its arrival at monitoring locations yields the breakthrough curves. The analysis of the breakthrough curves indicates the average arrival times of tracer gas, which relate to the positions of first breakthrough to the vadose zone, the dispersion of tracer gas and the heterogeneity of the flow domain. Under field conditions, the areal pattern of the tracer gas response is useful in defining multiple flow channels. The results of the tracer test, the numerical model and some simple mathematical equations are used to study the changes of porosity/permeability, the distribution of gas saturation and the ROI in a saturated zone during air sparging.

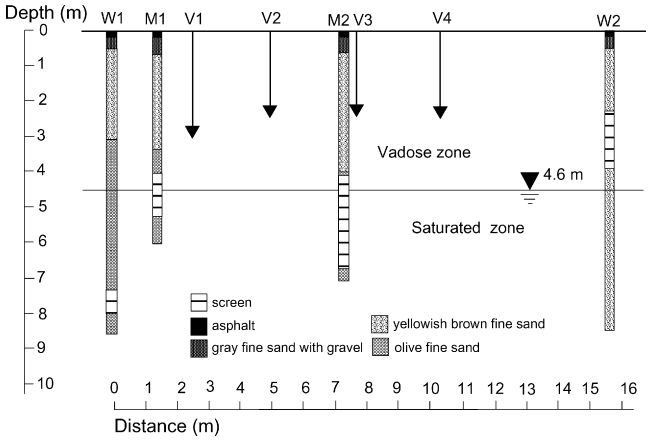

Fig. 1. Cross section and locations of the injection well, monitoring wells, soil vapor probes and soil vapor extraction well.

2. Experimental methods

2.1. Site description

Air sparging tests were performed at the Que-jen extended campus of National Cheng Kung University. This site is an artificial reparked site and the soil is constructed from sands and silts. It can be considered as an ideal and an extremely homogenous site. Moreover, this site is an unconfined system and four wells were installed in a 20-cm-diameter hole advanced by a cable tool rig. The wells were constructed from a 5-cm-diameter polyvinylchloride (PVC) pipe, W1 for air injection, W2 for extracting vapor from the vadose zone, and M1 and M2 for monitoring the groundwater (Fig. 1). The majority of the subsurface was fine sand to a depth of 8.5 m. According to the analyses of soil samples and slug tests performed on these four wells, the porosity of the soil ranged from 0.22 to 0.27 and the intrinsic permeability of the reservoir ranged from $0.75 \times 10^{-12} \pm 0.04 \times 10^{-12}\,m^2$ to $1.95 \times 10^{-12} \pm 0.09 \times 10^{-12}\,m^2$. Soil vapor probes (V), constructed of 0.5-cm-diameter polyethylene (PE) tubing, were located 2.6, 5.2, 7.8 and 10.4 m from the sparging well (Fig. 1).

2.2. In situ air sparging test

An oil-free compressor and an extraction pump were used to inject air and extract soil vapor (Fig. 2). Immediately after the air compressor was started up, the injection pressure rose to 56.5 kPa. Within 15 h, the injected pressure stabilized at approximately 27.6 kPa, and the injection flow rate stabilized at approximately 460 L/min. It is because when air was injected into groundwater, the resistances of air flow include the pressure head and the surface tension of water. When the air channels are formed and air flows steadily, the resistances of air flow will reduce evidently. In the SVE well, the negative gauge pressure was observed and stabilized at a vacuum of 13.7 kPa and the extraction flow rate stabilized at 580 L/min within

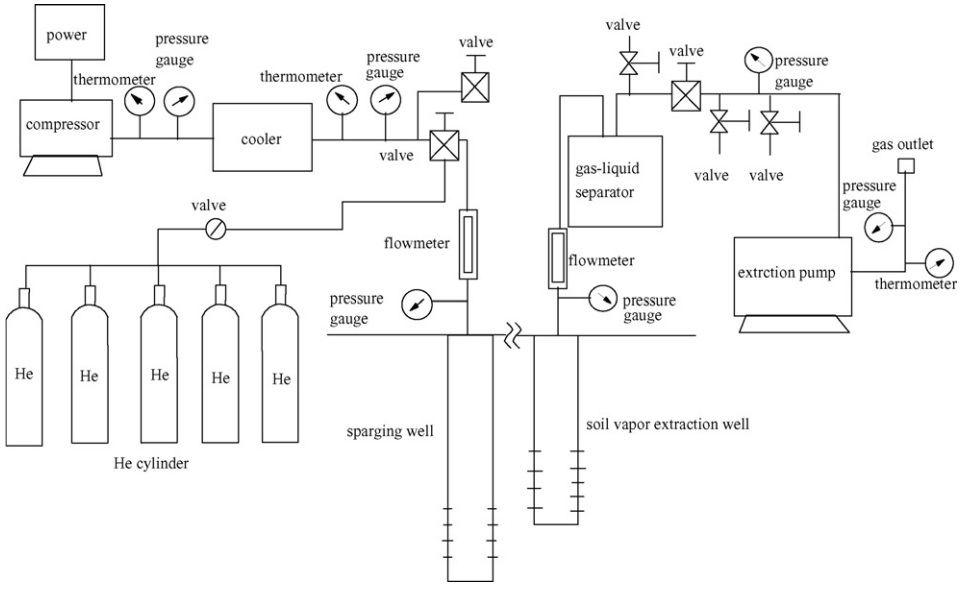

Fig. 2. Schematic in-situ air sparging and tracer test system.

2 h. The sparging events were operated in continuous flow for 5 days.

2.3. Tracer test

After air had been injected for 2 days, tracer gas (pure helium) was injected at the same flow rate as the injected air, following a pulse function. The total volume of injected tracer gas was 21,010 L and the ratio of the volume of helium to that of the total injected gas was 0.63%. After all of the tracer gas had been injected, air was injected in continuous flow for 3 days.

2.4. Sample analyses

Gas sampling and analyses were performed every 10–20 min. A portable air extractor was used to collect the soil gas from soil vapor probes. The air extractor was used with an in-line helium detector, and moved from probe to probe to perform the analyses. The helium detector used was a Helium Detector Model 9821 (Ashtead Technology), which uses a special sensor to directly detect the presence of helium. This detector measures concentrations from 0.01% to 100% with a method detection limit (MDL) of 0.009%. The duration of all gas sampling and analyses was 32 h.

2.5. Moment analysis

The breakthrough curves of a tracer gas can be used to understand the behavior of injected tracer gas transport through an aquifer. Time moment analysis of the breakthrough curve provides useful and physically meaningful descriptors of the concentration breakthrough [15]. In this study, the tracer gas data were analyzed by calculating the absolute zeroth moment and the normalized temporal first moment, to quantify the recovery and the mean travel time. The absolute zeroth moment (M_0) is defined as

$$M_0 = \int_0^\infty C(x, t)\,\mathrm{d}t \tag{1}$$

where t is time (min) and $C(x, t)$ is the concentration (%) as a function of space and time. The normalized temporal first moment (m_1) is defined as

$$m_1 = \frac{\int_0^\infty tC(x, t)\,\mathrm{d}t}{M_0} \tag{2}$$

2.6. Numerical model

The numerical model used in this study is the MORE (modular oil reservoir evaluation) reservoir model. This is a three-dimensional multi-component multiphase flow reservoir model, as described by Young and Stephenson [16,17]. This model applied the integral finite-difference method to perform spatial discretization and has been used to model the multiphase transport of such components as water, nitrogen, oxygen and tracer (helium) [18].

Flow rates, pressures, tracer injection data, fluid properties and the characteristics of the aquifer medium such as porosity, intrinsic permeability, relative permeability and capillary pressure were used as inputs to the model (Table 1).

Table 1
Multiphase flow parameters for air sparging simulations

Porosity	0.22–0.27
Permeability (m^2)	7.5×10^{-13} to 1.95×10^{-12}
Well diameter (cm)	5
Injected pressure (kPa)	27.6
Air (helium) flow rate (L/min)	460
Extraction pressure (vacuum of, kPa)	13.7
Extraction flow rate (L/min)	580
Reservoir temperature (°C)	20
Residual water saturation	0.15
n (relative permeability functions)	3[a]
α_{gw}	5.2[a]
S_m	0.0[a]
n (capillary pressure functions)	1.84[a]

[a] From Ref. [3] for sandy medium.

Capillary pressure is an important variable which affects the multiphase flow phenomena associated with air sparging. In the present work, the two-phase method developed by van Genuchten [19], are used:

$$P_{cgw} = \frac{\rho_w g}{\alpha_{gw}}\left[\left(\frac{S_w - S_m}{1 - S_m}\right)^{-1/m} - 1\right]^{1/n} \tag{3}$$

where P_{cgw} is the gas–water capillary pressure (Pa), α_{gw} (m^{-1}) and S_m are empirically determined and are assumed to be constants of the porous medium, g the gravitational acceleration (9.801 m/s^2) and m is an empirically determined constant which equals $1 - n^{-1}$.

The relative permeability for the gas and aqueous phases is assumed to be a power function of the respective phase saturation. And the widely accepted and commonly used functions of Fatt and Klickoff [20], in which relative permeability for a phase is a cubic function of that phase's saturation, are used. The formulations used are as follows:

$$K_{rw} = \left[\frac{S_w - S_{wr}}{1 - S_{wr}}\right]^n \tag{4}$$

$$K_{rg} = \left[\frac{S_g}{1 - S_{wr}}\right]^n \tag{5}$$

where K_{rw} is the relative permeability of aqueous phase, S_w the saturation of aqueous phase, S_{wr} the residual saturation of aqueous phase, n equals 3, K_{rg} the relative permeability of gas phase and S_g is the saturation of gas phase.

2.7. Adjustment of model parameters

This study assumed that soil particles simply move with water. Some previous studies have described the relationship between the water flow rate and soil particle movement [5–7,21,22]. Additionally, El-Farhan et al. [22] demonstrated that the cumulative number of particles collected during the infiltration experiments depended linearly on the cumulative water volume collected.

At the start of air sparging in the saturated zone, the injected air displaces the water. The displacement of water flow causes movement of soil particles in the porous medium. Soil particle movement was observed during the initial stage of air-channel development [5]. To establish the equation of the increase in porosity, a representative elemental volume (V_e) in the saturated zone is considered. At the beginning, the injected gas displaces the water in the porous medium and induces particle movement. The gas volume in porous (V_g) equals the sum of the water volume displaced (V_w) and the volume of moved particles (V_p).

$$V_g = V_w + V_p \tag{6}$$

Applying the results of El-Farhan, the cumulative mass of moved particles (M_p) is assumed to be proportional to the volume of water displaced, as follows:

$$\frac{M_p}{V_w} = E \tag{7}$$

where E is a constant. Moreover, the cumulative volume of moved particles is proportional to the cumulative mass of moved particles as follows:

$$V_p = \frac{M_p}{\rho_p} \tag{8}$$

where ρ_p is the bulk density of the soil particle.

The gas saturation (S_g) in the representative elemental volume with a volume of gas injected is as follows:

$$S_g = \frac{V_g}{V_e} = \frac{V_w + V_p}{V_e} \tag{9}$$

The increase in porosity resulting from the particle movement from the representative elemental volume (V_e) is as follows:

$$\Delta\phi = \frac{V_p}{V_e} \tag{10}$$

Substituting Eq. (9) into Eq. (10), the increase in porosity can be written as follows:

$$\Delta\phi = \frac{V_p}{V_w + V_p} \times S_g \tag{11}$$

Substituting Eqs. (7) and (8) into Eq. (11), the increase in porosity can be expressed as follows:

$$\Delta\phi = C \times S_g \tag{12}$$

where C is a constant and equals $E/(\rho_p + E)$.

The increase in porosity changes the permeability of the soil. Some models have described the effect of porosity by defining permeability as follows [23]:

$$K = C_s f(\phi) d_{50}^2 \tag{13}$$

where K is the permeability of the porous medium (m^2); C_s a constant; $f(\phi)$ a function of the porosity of the porous medium and d_{50} is the mean size of the soil particles (m). The general form of $f(\phi)$ is

$$f(\phi) = \frac{\phi^3}{(1-\phi)^2} \tag{14}$$

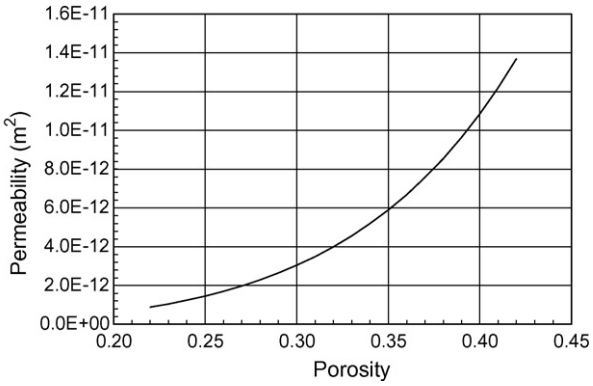

Fig. 3. Relationships between permeability and porosity (calculated from Eqs. (13) and (14)).

Eqs. (13) and (14) generally apply to sandy soil. Eq. (13) can be used to determine the constant C_s from given field data on permeability, porosity and the mean size of the soil particles. In this study, C_s was 0.0031 ± 0.0004, which is within the expected range for a sandy material with grains smaller than 0.5 mm [24]. Fig. 3 plots the relationships between permeability and porosity, following Eqs. (13) and (14), for a constant C_s and diverse porosities.

The procedures for correcting parameters used herein are as follows: (1) obtain the gas saturation contour maps of the reservoir by inputting the unrevised site parameters into the model; (2) determine the increases in the porosity of soil from Eq. (12) and the gas saturation contour maps from the prior model output; (3) obtain the revised permeability from Fig. 3 and the revised porosity data; (4) use the revised site parameters in the model to determine the simulated breakthrough curves of the tracer gas at the soil vapor probes and the gas saturation contour maps following the simulations.

3. Results

3.1. Change in porosity and permeability

Using the original gas saturation contour map of the saturated zone and Eq. (12), Fig. 4 shows the change in the predicted porosity of the soil after sparging for $C = 0.10$ as an example. The maximum change in predicted porosity is 0.07, ranging from 0.27 to 0.34, near the well (W1) screen. Based on the relationship between porosity and permeability in Fig. 3 and when $C = 0.10$, the maximum permeability change ranges from 1.95×10^{-12} to 5.26×10^{-12} m^2 near the well (W1) screen, and the maximum percentage increases in porosity and permeability are 26% and 170%, respectively.

3.2. Observed and simulated breakthrough curves

Fig. 5 plots the breakthrough curves of the field tracer test and the corresponding curves simulated for different values of the constant C in Eq. (12). The breakthrough curves exhibit tailing. The tailing is likely to be related to the flow field associated with the single sparging and the single extraction well couplet in an

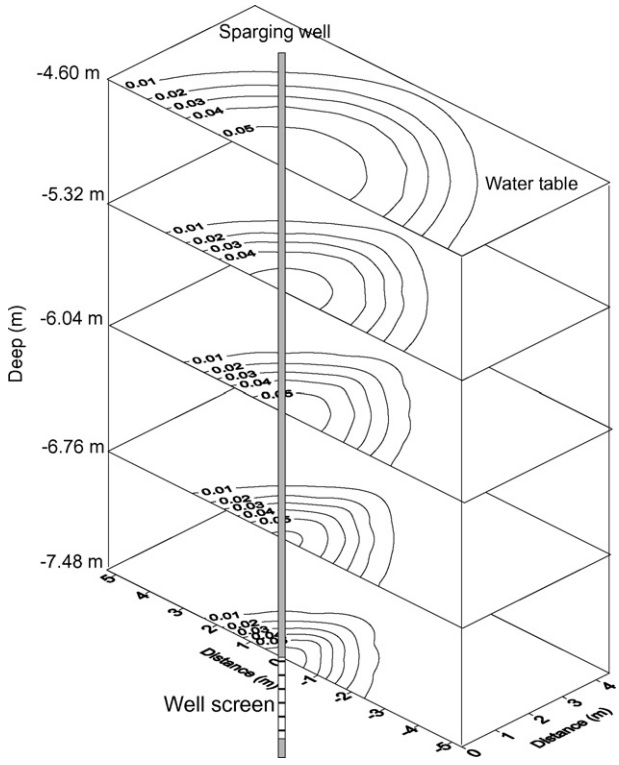

Fig. 4. Change of soil porosity with depth during air sparging test ($C = 0.10$).

open system; the extraction pump cannot extract the injected gas efficiently and some gas is trapped within the pores. Table 2 shows the moment analyses of breakthrough curves for the field data and simulation results.

3.3. Breakthrough curves of soil vapor probe V1

At soil vapor probe V1, a helium response was observed within 10 min of startup, as shown in Fig. 5(a). Besides, Fig. 5(a) shows the curves simulated for $C = 0.00$, 0.05, 0.06, 0.07, 0.08, 0.09, 0.10, 0.11, 0.13, 0.15 and 0.20. The model could not account for all of the field phenomena due to the preferential flow during the air sparging test. The results of moment analysis in Table 2 and Fig. 5(a) indicate that most of the air channels (or main air channels) were concentrated around the sparging well (W1). According to the mean linear pore gas velocity ($v_{0,1}$) between W1 and V1, the horizontal distance was approximately 0.2 m between V1 and the nearest break point of the main air channels. Varying C above 0.00 does not change the model outputs significantly. However, when C is not 0.00, the model fits the data slightly better, but none of the simulations fitted the data well. The mean travel time of helium is shorter than predicted by the model. However, the absolute zeroth moments of the simulated breakthrough curves are all close to that of the actual breakthrough curve. The absolute zeroth moments of the simulated breakthrough curves represent the mass of tracer gas. This result reveals that the mass balance is matched between field data and simulation results in soil vapor probe V1.

3.4. Breakthrough curves of soil vapor probe V2

Fig. 5(b) shows the tracer breakthrough data and the results of the numerical simulation for the soil vapor probe V2. The model fit data at V2 better than data at V1. According to the field data, a peak is present in the field data at approximately

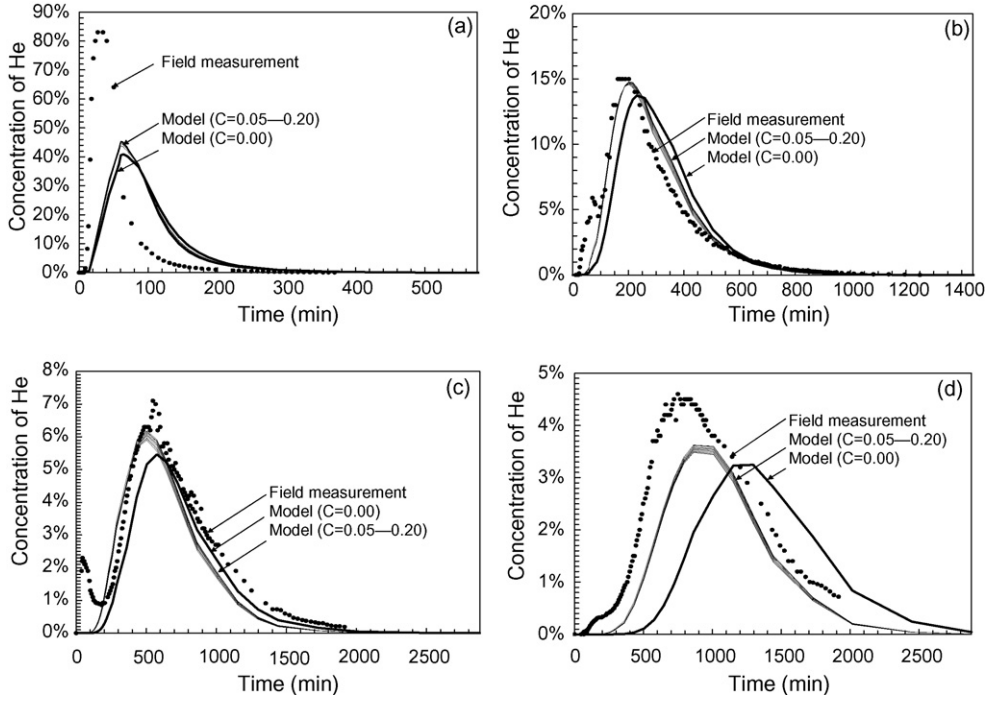

Fig. 5. Tracer breakthrough curves obtained by field measurements and numerical simulation: (a) at soil vapor probe V1, (b) at soil vapor probe V2, (c) at soil vapor probe V3 and (d) at soil vapor probe V4.

Table 2
Results of moment analysis

Soil vapor probe	V1	V2	V3	V4
Actual data				
Absolute zeroth moment (min)	41.85	41.52	45.58	44.27
Mean travel time (min), t_n	52.10	283.72	703.27	1029.48
Mean linear pore gas velocity (m/min) $v_{n-1,n} = (x_n - x_{n-1})/(t_n - t_{n-1})$	$v_{0,1} = 0.0331$[a]	$v_{1,2} = 0.0112$	$v_{2,3} = 0.0062$	$v_{3,4} = 0.0092$
$C = 0.00$				
Absolute zeroth moment (min)	40.08	41.04	34.75	33.34
Mean travel time (min)	101.31	325.29	744.47	1396.05
$C = 0.05$				
Absolute zeroth moment (min)	39.26	40.54	35.61	30.29
Mean travel time (min)	94.09	292.64	641.17	1070.43
$C = 0.06$				
Absolute zeroth moment (min)	39.51	40.85	35.85	30.48
Mean travel time (min)	94.04	294.02	643.89	1072.94
$C = 0.07$				
Absolute zeroth moment (min)	39.78	41.20	36.12	30.70
Mean travel time (min)	94.12	295.27	646.57	1074.82
$C = 0.08$				
Absolute zeroth moment (min)	40.05	41.56	36.42	30.93
Mean travel time (min)	94.30	296.37	648.59	1076.26
$C = 0.09$				
Absolute zeroth moment (min)	40.28	41.89	36.67	31.13
Mean travel time (min)	94.42	297.61	650.65	1077.89
$C = 0.10$				
Absolute zeroth moment (min)	40.47	42.17	36.90	31.32
Mean travel time (min)	94.65	298.17	651.65	1078.52
$C = 0.11$				
Absolute zeroth moment (min)	40.61	42.38	37.01	31.50
Mean travel time (min)	94.84	298.75	652.55	1079.02
$C = 0.13$				
Absolute zeroth moment (min)	40.69	42.60	37.37	31.78
Mean travel time (min)	95.30	299.41	652.58	1077.96
$C = 0.15$				
Absolute zeroth moment (min)	40.74	42.75	37.61	32.00
Mean travel time (min)	95.91	299.86	651.94	1076.59
$C = 0.20$				
Absolute zeroth moment (min)	40.73	42.88	37.89	32.25
Mean travel time (min)	97.17	299.57	649.38	1075.38

[a] Estimated from the mean travel time of $C = 0.00$ and the distance between wells W1 and V1.

71 min, indicating that a preferential air channel broke from the saturated zone into the vadose zone between V1 and V2. The moment analysis revealed that the horizontal distance between this breakthrough point and V2 is 0.8 m and this air channel appeared just for approximately 5 min. The results of moment analysis (Table 2) show that simulated data for $C > 0.00$ were better than simulated data for $C = 0.00$, especially for mean travel time, but the model was insensitive to $C > 0.00$.

3.5. Breakthrough curves of soil vapor probe V3

Fig. 5(c) shows the tracer breakthrough data and the results of the numerical simulation for the soil vapor probe V3. The field data showed a significant peak at approximately 46 min, indicating that a breakthrough point of preferential air channel was between V2 and V3. This channel appeared only for approximately 2 min. The horizontal distance between this breakthrough point and V3 is approximately 0.3 m. The results of moment analysis (Table 2) show that the absolute zeroth moment for the field data was greater than that of V1 and V2, and was also substantially greater than those of the simulated curves. Two possible reasons may account for this phenomenon: first, there is an effect of preferential air channels that did not flow through V1 and V2, but flowed through V3, as shown by the minor peak in Fig. 5(c). Second, the unknown geological heterogeneities during air sparging made it difficult to precisely determine the mass recovery under field conditions. Simulated results for $C > 0.00$ were not better obviously than those for $C = 0.00$. Moreover, varying C above 0.00 did not distinguishably change the model outputs.

3.6. Breakthrough curves of soil vapor probe V4

Fig. 5(d) shows the breakthrough data and the results of the numerical simulation for the soil vapor probe V4. A slight hump is observed at approximately 180 min perhaps due to a minor preferential air channel that broke into the vadose zone between V3 and V4. The horizontal distance from this breakthrough point to V4 was estimated at about 1.7 m. Also, the hump may be related to a preferential flow channel between V2 and V3, as shown in Fig. 5(c). The results of moment analysis (Table 2) show that the simulated breakthrough curve for $C = 0.00$ clearly lags that obtained from field measurements at V4. Adjusting the porosity and permeability of the soil yielded a significant improvement in the model fit to the tracer data, especially in terms of the mean travel time. With regard to mass recovery, for the same reasons as applied at V3, the absolute zeroth moments of the simulated curves are lower than those of the field data.

4. Discussion

4.1. Air flow during in situ air sparging

Ji et al. [2] found that in medium to fine-grained water saturated porous media, air flows in discrete channels. With a vertical air sparging well, the network of air channels formed may be visualized as the roots of a tree [25]. It is well known that the injected air travels within discrete channels during air sparging. Nevertheless, this study obtains some special finding about the air channels. The tracer and simulated breakthrough curves in Fig. 5 indicate that (1) preferential air channel flow occurred during air sparging and the main air channels were concentrated in a area around the sparging well with a radius of less than 2.6 m; (2) some minor preferential air channels were present outside of the main air channels when the tracer gas began to be injected, and that these channels appeared for just a short period; (3) some minor preferential air channels did not flow through V1 and V2, so the recoveries of V3 and V4 exceeded those of V1 and V2.

It is because that the saturated zone offered some less resistant flow paths near the sparging well, after the permeability increased. Hence, the air channels concentrated in the zone with greater permeability. This phenomenon can reasonably interpret the changes in air flow paths and the disappearances of some preferential air channels. Moreover, the result of numerical model also reveals that adjusting the porosity and permeability near the sparging well broadly improved the breakthrough curve simulations. This result also can demonstrate the increase in porosity and permeability near the sparging well.

4.2. Particles movement during in situ air sparging

The monitoring well M1 is near the air sparging well and is screened across the water table. This well represents a path for short-circuiting during air sparging, namely, air flowing into the vadose zone via the well will encounter less resistance than air passing through soil. If soil particles could be transported by the flowing water, they could be flushed into this well. After air sparging, mud was found in the well. The mud, which consisted of fine sand (81.32% particles had grain sizes of under 0.1 mm, and a mean size of 0.071 mm), was likely transported into the well tube by flowing water. These results suggest that the initial displacement of water by air produces the bulk of the observed particle mobilization. However, this phenomenon was not observed at monitoring well M2, probably because only a few brief minor air channels flowed to M2. Shear theory dictates that a decrease in porosity implies that some particles are deposited in the voids of the soil around the water table [5] or in an area with a relatively low water flow rate, e.g. some particles were found to deposit in M1.

4.3. Influence of porosity change on ROI

Based on the model output data, Fig. 6 shows the distribution of gas saturation around the sparging well before and after a correction value of $C = 0.10$ was used in the simulation. The model simulation revealed a decrease in the swept volume and the ROI.

Since most of the particles were transported during the first few hours of flow [21,22], the screen of M1 may have been blocked when the tracer test was conducted. Hence the limitation on the ROI of injected tracer gas could be neglected. The most probable reason for the decline in the ROI is that the air channels concentrated in the zone with greater permeability. Tracer breakthrough curves in Fig. 5 also show the disappearance of some minor preferential air channels. This finding also indicates the concentrating in the air channels and a fall in the swept volume.

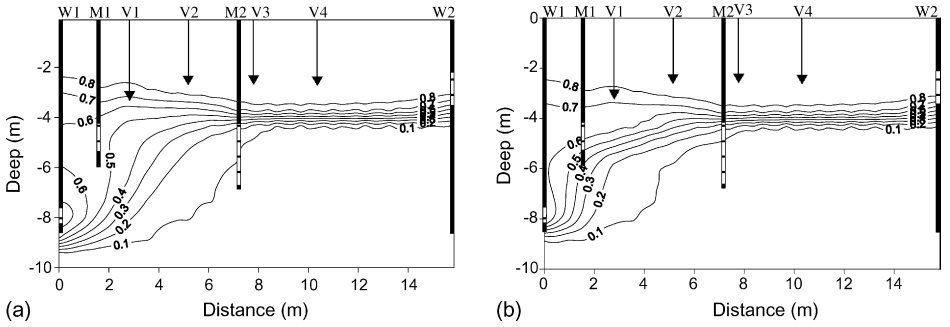

Fig. 6. Distribution of the saturation of gas around sparging well: (a) before the data were revised ($C = 0.00$) and (b) after the data were revised ($C = 0.10$).

4.4. Validation of results

A slug test was performed on the air sparging well (W1) to evaluate the change in permeability due to the air sparging test. The permeabilities of W1 are $1.95 \times 10^{-12} \pm 0.09 \times 10^{-12}$ m^2 before air sparging and $3.39 \times 10^{-12} \pm 0.16 \times 10^{-12}$ m^2 nine days after air sparging, respectively. The increase in the soil permeability around W1 may indicate an increase in porosity according to Eqs. (13) and (14). According to Fig. 3, the average porosity around the well screen of W1 was estimated at about 0.31 following air sparging. Therefore, this air sparging test increased the porosity near the well screen of W1 by approximately 0.04. Transport of particles away from the sparging well could explain the increase in porosity and permeability.

5. Conclusions

This study develops methods by combined in situ air sparging and tracer testing, and comparing the breakthrough curves obtained from the tracer gas with those obtained by a numerical simulation model. These methods successfully estimate the change in soil characteristics and associated air flow paths in a saturated zone during in situ air sparging. The results reveal some special finding about the air channels and extend our understanding of the air channel behavior. The following observations can be made regarding the developed methods:

1. Preferential air channel flow occurred during air sparging and the main air channels were concentrated in an area around the sparging well.
2. Some minor preferential air channels were present outside of the main air channels when the tracer gas began to be injected, and that these channels appeared for just a short period.
3. The disappearances of some air channels revealed a decrease in the swept volume and the ROI.
4. Some minor preferential air channels did not flow through the soil vapor probe near the sparging well, so the recoveries of V3 and V4 exceeded those of V1 and V2.

The result of numerical model reveals that increasing the porosity and permeability near the sparging well broadly improved the breakthrough curve simulations. Moreover, some particles being found to deposit in M1 and the increase in soil permeability around W1 are both direct evidences that soil particles were transported and altering the permeability. This phenomenon can reasonably interpret the changes in air flow paths and the disappearances of some preferential air channels.

Revising the porosity and permeability according to the distribution of gas saturation is helpful in breakthrough curve fitting. However, these changes are unable to account for the effects of preferential air flow paths, especially in the zone closest to the points of air injection. Since the effected of preferential air flow pathways on tracer breakthrough curves could not be reproduced by the model, and the extent to which these pathways are affected by the air sparging treatment is not known, further study of this phenomenon is required.

Acknowledgments

The authors would like to thank the National Science Council of the Republic of China, Taiwan for financially supporting this research under Contract NSC 90-2218-E-434-001. Dr. Hueyhong Hsieh and Dr. Ming-Ching Tom Kuo are also greatly appreciated for her editorial review.

References

[1] S.E. Burns, M. Zhang, Effects of system parameters on the physical characteristics of bubbles produced through air sparging, Environ. Sci. Technol. 35 (2001) 204–208.
[2] W. Ji, A. Dahmani, D.P. Ahlfeld, J.D. Lin, E.H. Hill III, Laboratory study of air sparging: air flow visualization, Ground Water Monit. Rem. 13 (1993) 115–126.
[3] J.E. McCray, R.W. Falta, Defining the air sparging radius of influence for groundwater remediation, J. Contam. Hydrol. 24 (1996) 25–52.
[4] J.E. McCray, R.W. Falta, Numerical simulation of air sparging for remediation of NAPL contamination, Ground Water 35 (1997) 99–110.
[5] Y.J. Tsai, D.F. Lin, Mobilizing particles in a saturated zone during air sparging, Environ. Sci. Technol. 38 (2004) 643–649.
[6] D.I. Kaplan, P.M. Bertsch, D.C. Adriano, W.P. Miller, Soil-borne mobile colloids as influenced by water flow and organic carbon, Environ. Sci. Technol. 27 (1993) 1193–1200.
[7] D.I. Kaplan, M.E. Summer, P.M. Bertsch, D.C. Adriano, Chemical conditions conductive to the release of mobile colloids from Ultisol profiles, Soil Sci. Soc. Am. J. 60 (1996) 269–274.
[8] A.G. Noack, C.D. Grant, D.J. Chittleboroough, Colloid movement through stable soils of low cation-exchange capacity, Environ. Sci. Technol. 34 (2000) 2490–2497.
[9] M.I.J. van Dijke, S.E.A.T.M. van der Zee, C. van Duijn, Multi-phase flow modeling of air sparging, Adv. Water Resour. 18 (1995) 319–333.
[10] P.D. Lundegard, G. Andersen, Multiphase numerical simulation of air sparging performance, Ground Water 34 (1996) 451–460.
[11] J.R. Philip, Full and boundary-layer solutions of the steady air sparging problem, J. Contam. Hydrol. 33 (1998) 337–345.
[12] M.I.J. van Dijke, S.E.A.T.M. van der Zee, Modeling of air sparging in a layered soil: numerical and analytical approximations, J. Geophys. Res. 34 (1998) 341–353.
[13] A.J. Rabideau, J.M. Blayden, Analytical model for contaminant mass removal by air sparging, Ground Water Monit. Rem. 18 (1998) 120–130.
[14] D.J. Wilson, S. Kayano, R.D. Mutch Jr., A.N. Clarke, Groundwater cleanup by in-situ sparging. I. Mathematical modeling, Sep. Sci. Technol. 27 (1992) 1023–1041.
[15] A.J. Valocchi, Validity of the local equilibrium assumption for modeling sorbing solute transport through homogeneous soils, Water Resour. Res. 21 (1985) 808–820.
[16] L.C. Young, Full-field compositional modeling on vector processors, SPE Reservoir Eng. (1991) 107–114.
[17] L.C. Young, R.E. Stephenson, A generalized compositional approach for reservoir simulation, Soc. Pet. Eng. J. (1983) 727–742.
[18] Y.J. Tsai, M.C.T. Kuo, T.S.E. Huang, Air sparging tracer test to investigate the flow path, J. Environ. Sci. Health, Part A A36 (2001) 999–1014.
[19] M.Th. van Genuchten, A review of immiscible fluids in the subsurface: properties, models, characterization and remediation, Soil Sci. Soc. Am. J. 44 (1980) 892–898.
[20] I. Fatt, W.A. Klickoff, Effect of fractional wettability on multiphase flow through porous media, AIME Trans. 216 (1959) 216–246.
[21] Y.H. El-Farhan, N.M. Denovio, J.S. Herman, G.M. Hornberger, Mobilization and transport of soil particles during infiltration experiments in an agricultural field, Shenandoah Valley Virginia, Environ. Sci. Technol. 34 (2000) 3555–3559.
[22] N. Weisbrod, O. Dahan, E.M. Adar, Particle transport in unsaturated fractured chalk under arid conditions, J. Contam. Hydrol. 56 (2002) 117–136.

[23] B.B. Rajani, A simple model for describing variation of permeability with porosity for unconsolidated sands, In Situ 12 (1988) 209–226.
[24] M. Vukovic, A. Soro, Determination of Hydraulic Conductivity of Porous Media from Grain-size Composition, Water Resources Publications, Littleton, Colorado, 1992, 83 pp.
[25] A.S. Drucker, S.S. Di Julio, Groundwater cleanup, in situ air sparging: development of a model and application to saturated soil column experiments, in: Proceedings of 69th Annual Conference and Exposition of the Water Environmental Federation, Dallas, TX, 5–9 October, 1996.